Carbon 96 (2016) 1–9

Contents lists available at ScienceDirect

Carbon

journal homepage: www.elsevier.com/locate/carbon

Detecting carbon in carbon: Exploiting differential charging to obtain information on the chemical identity and spatial location of carbon nanotube aggregates in composites by imaging X-ray photoelectron spectroscopy

Justin M. Gorham [a, *], William A. Osborn [a], Jeremiah W. Woodcock [a], Keana C.K. Scott [a], John M. Heddleston [b], Angela R. Hight Walker [b], Jeffrey W. Gilman [a]

[a] Material Measurement Laboratory, National Institute of Standards and Technology, 100 Bureau Drive, Gaithersburg, MD 20899, USA
[b] Physical Measurement Laboratory, National Institute of Standards and Technology, 100 Bureau Drive, Gaithersburg, MD 20899, USA

ARTICLE INFO

Article history:
Received 26 August 2015
Received in revised form
15 October 2015
Accepted 21 October 2015
Available online 24 October 2015

ABSTRACT

To better assess risks associated with nano-enabled products including multiwalled carbon nanotubes (MWCNT) within polymer matrices, it is important to understand how MWCNT are dispersed throughout the composite. The current study presents a method which employs imaging X-ray photoelectron spectroscopy (XPS) to chemically detect spatially segregated MWCNT rich regions at an epoxy composites surface by exploiting differential charging. MWCNT do not charge due to high conductivity and have previously been shown to energetically separate from their insulating surroundings when characterized by XPS. XPS in imaging mode revealed that these conductive regions were spatially separated due to micrometer-scale MWCNT aggregation and poor dispersion during the formation of the composite. Three MWCNT concentrations were studied; (1, 4 and 5) % by mass MWCNT within an epoxy matrix. Images acquired in periodic energy intervals were processed using custom algorithms designed to efficiently extract spectra from regions of interest. As a result, chemical and electrical information on aggregate and non-aggregate portions of the composite was extracted. Raman imaging and scanning electron microscopy were employed as orthogonal techniques for validating this XPS-based methodology. Results demonstrate that XPS imaging of differentially charging MWCNT composite samples is an effective means for assessing dispersion quality.

Published by Elsevier Ltd.

1. Introduction

Incorporation of nanomaterials into composites has led to the development of novel products and innovations due to the improved physico-chemical properties that are imparted by the nanoscale filler. For example, incorporating carbon nanotubes (CNT) into polymers generates composites, which are sought after for benefits including enhanced mechanical strength [1–4], favorable electrical conductivity [3–11], and lower overall mass [3]. Indeed, a search of The Project for Emerging Nanotechnologies[1] consumer product inventory revealed 38 products claiming to contain CNT, many incorporated into electronics, plastics, epoxies, resins, or adhesives, and other reviews have demonstrated a comparable use of CNT elsewhere [12]. Therefore, it is unsurprising that there has been an increase in CNT production along with research and publications on the topic [13]. Due to the increasing number of nano-containing products, an environmental, health, and safety research strategy was developed by the National Nanotechnology Initiative which highlights the need to develop measurement infrastructure, including tools and methods, to provide effective characterization of nanomaterials in consumer products towards informed risk assessment[2] [13]. Therefore, composites of CNT in epoxy have been selected as a relevant model system for development of physical and chemical characterization and detection techniques in the current study.

One technique well suited towards characterization of nanomaterials in and out of composites is X-ray photoelectron

* Corresponding author.
E-mail address: justin.gorham@nist.gov (J.M. Gorham).

[1] www.nanotechproject.org/inventories/consumer/analysis_draft/.

[2] http://www.whitehouse.gov/sites/default/files/microsites/ostp/nni_2011_ehs_research_strategy_final.pdf.

http://dx.doi.org/10.1016/j.carbon.2015.10.073
0008-6223/Published by Elsevier Ltd.

spectroscopy (XPS) [14,15]. XPS is a surface sensitive technique (analysis depth ≈ 10 nm) which provides qualitative to quantitative information on the concentration of surface atoms and their local chemical environment (*e.g.*, oxidation state) [16]. For example, XPS has been employed in the elemental analysis of silica nanoparticles (SiNP) in epoxy matrices to better understand surface transformation due to environmental factors such as ultraviolet light (UV) degradation [17–20]. Similarly, XPS has been employed to characterize the chemical composition of textiles, composites and thin films prepared from silver nanoparticle suspensions [21–24].

However, the primary measurement challenge one faces in using XPS to characterize CNT dispersed in an epoxy composite is attempting the simultaneous measurement of carbon in two different chemical states [25]. Furthermore, comparing the literature for CNT and polymeric hydrocarbon reveals that the C(1s) spectral features have a high degree of overlap making identification by traditional peak fitting challenging [25–27]. Regardless, there have been several attempts to separate the signals of graphitic carbon and hydrocarbon by peak fitting analysis within composites [6,9,28]. Recently, XPS characterization of a CNT: poly(vinyl alcohol) (PVA) composite series was effectively demonstrated using peak fitting by taking advantage of minor differential charging to calculate the relative surface percentage of carbon species from nanofiller and matrix material [28]. Other approaches have employed XPS imaging through analysis of the carbon Auger feature to differentiate graphitic carbon (sp^2 hybridized) from an adhesive carbon (sp^3 hybridized) background (comparable with CNT and polymeric carbon, respectively) to spatially separate different carbon components [29].

In XPS, differential charging is observed when a heterogeneous material with at least two components of differing electrical properties are exposed to sufficient X-rays to experience a net electron flux [25,30,31]. As a result of this imposed current, less conductive components of a composite will develop a positive bias, also known as charging. This charging decreases the kinetic energy of photoelectrons emitted from an insulating surface. The effects of charging may include shifts in the binding energy of spectral peaks [31–33] or a complete loss of spectral features associated with extremely non-conductive materials [20,34]. However, MWCNT, polymers and their composites are known to have very different electrical properties which has the potential to lead to differential charging [35–39]. Differentially charging samples will also have a surface component that is more conductive, resulting in photoelectrons emitted at a kinetic energy more closely associated with their originating orbitals. This complicates chemical characterization, which depends on having one energy scale to differentiate between binding energy shifts in order to identify different chemical functionalities. Generally, differential charging is considered to be undesirable for XPS. However, this normally undesirable effect can have positive outcomes.

This phenomenon has recently been used at NIST to spectrally separate the two carbon-based components in multiwall CNT (MWCNT) composites based on their electrical properties [34]. In that study, we exploited differential charging in XPS to obtain spectra with energetically separated features for the MWCNT and the epoxy-rich matrix components as a result of surface enrichment of MWCNT due to UV weathering of the composite and removal of the polymer. This separation in spectral line shapes was subsequently observed in other comparable studies and in surface-modified MWCNT composites [25]. However, an unresolved question from the previous study was whether or not the differential charging that occurred was due to dispersion properties within the composite. The current study demonstrates how imaging XPS can be employed to directly assess the dispersion properties of MWCNT composites by energetically separating overlapping carbon signals through differential charging to spatially identify MWCNT-rich regions.

To this end, composite samples of varying MWCNT loading have been prepared and characterized using XPS in spectroscopy and imaging modes. Samples composed of MWCNT composites were prepared for XPS by mechanically removing the top surface layer. MWCNT composites were studied via XPS imaging to determine if this method could be used to detect localized MWCNT rich regions. XPS spectra were extracted using a novel image analysis procedure which identified and collected signal from spatially unique chemical features in a series of images. Scanning electron microscopy (SEM) and Raman mapping were also employed as orthogonal measurements to validate the presence of MWCNT rich regions identified by XPS imaging. Results from these measurements demonstrate the utility of XPS imaging with differential charging in identifying MWCNT composites by separating carbon signals both spectrally and spatially based on differential charging.

2. Experimental[3]

2.1. MWCNT composite and control preparation

The creation of MWCNT composites using a two part epoxy has been discussed in the literature [28,34,40]. The MWCNT employed in this study were from Arkema (King of Prussia, PA). The epoxy matrix was composed of diglycidal ether of bisphenol A (Sigma Aldrich) and a mixture of polyether diamine curing agent (90% by mass Jeffamine d230; 10% by mass Jeffamine d2000, Huntsman, Pensacola, FL). The raw MWCNT were dispersed in the curing agent using a dual asymmetric centrifugal shear mixer (FlackTek, Landrum, SC) operating at 366.52 rad/sec (3500 rotations per min (RPM)) for 5 min. The epoxy monomer was added and the suspension was then mixed for an additional 20 min at 3500 RPM. The samples were degassed under vacuum at 80 °C for 10 min then poured into silicone molds and cured at 80 °C for 2 h. Samples were made with 1%, 4% and 5% MWCNT loadings by mass and will henceforth be referred as 1%, 4% and 5% MWCNT composites. Control samples consisted of separate measurements of as received MWCNT adhered on copper tape and a sample of the cured, two-component epoxy using the same materials as previously mentioned.

2.1.1. Surface preparation of MWCNT composites

Most composite surfaces were modified prior to analysis to remove the surface layer which is known to be rich in epoxy [17,34]. This was achieved by milling the composite surface mechanically using a Sherline Model 2000 mill (Vista, California). The process was performed in an enclosed chamber with a HEPA filter equipped vacuum nozzle which was directed at the milled surface to collect removed particles. The exception to this was the 4% sample shown in Fig. 6 which was prepared using a Leica Microsystems (Buffalo Grove, IL) EM TXP milling tool which also mechanically removed 10's to 100's of micrometers of the topmost surface layer.

2.2. X-ray photoelectron spectroscopy (XPS)

XPS data were collected on an Axis Ultra DLD from Kratos

[3] Certain commercial entities, equipment or materials may be identified in this document in order to describe an experimental procedure or concept adequately. Such identification is not intended to imply recommendation or endorsement by the National Institute of Standards and Technology (NIST), nor is it intended to imply that the entities, materials or equipment are necessarily the best available for the purpose.

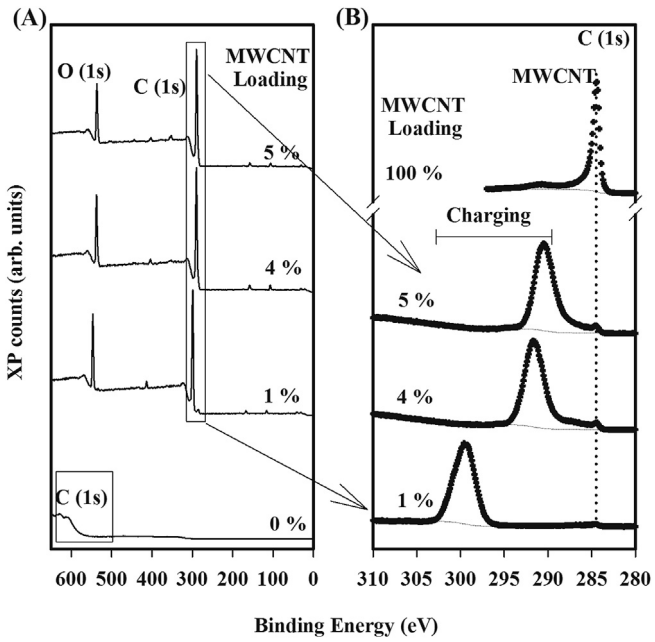

Fig. 1. XP spectra of the MWCNT composites demonstrate the insulating effect of epoxy. (A) Spectra reveal a drastic charge induced shift in the epoxy spectra (0%) compared to nominally (1, 4 and 5) % by mass MWCNT. NOTE: The boxed regions represent the C(1s) peak location. (B) High resolution spectra reveal a differentially charging composite characterized by a static 'MWCNT' peak and a shifting 'charging' peak. A MWCNT control is also provided as a reference and is scaled down by a factor of 16.8 for ease of viewing.

Analytical (Chestnut Ridge, NY). Prior to data acquisition, MWCNT composites were mounted onto a sample bar, fastened to the surface by metal straps and placed in a load lock chamber for pump down. Upon achieving a sufficient vacuum ($P < 2.7 \times 10^{-5}$ Pa (2×10^{-7} torr)), the samples were transferred into the main chamber ($P_{base} < 2.7 \times 10^{-7}$ Pa (2×10^{-9} torr)).

Spectroscopy based measurements were performed using monochromatic Al Kα X-rays ($h\nu = 1486.6$ eV) generated at a power of 150 W (10 mA; 15 kV). This X-ray source was employed to observe spectral features free of any artifacts induced by X-ray satellites. Samples were z-adjusted by maximizing the C(1s) photoelectron intensity while the surface was charge neutralized using a low energy electron flood gun. After height adjustments, the charge neutralizer was turned off unless otherwise mentioned and photoelectrons were analyzed over a wide range at pass energy 160 eV for survey spectra and over a small range at pass energy 40 eV for high energy resolution, C(1s) spectra. The area of analysis was set by using hybrid mode and slot aperture with 90% of the signal being collected from a 0.94 mm × 2.25 mm area, as previously determined [41]. Spectra were processed using CasaXPS and were fit with Shirley backgrounds. There were no energy corrections made after collection of the data in any of the presented spectra. Peak positions reported are the average and 1 standard deviation of 3 separate measurements.

XPS images were acquired on the same sample set that was analyzed in spectroscopy mode and were 256 pixels × 256 pixels in dimensions. Unless otherwise mentioned, imaging was conducted using Mg Kα X-rays ($h\nu = 1253.6$ eV) generated at a power of 405 W (27 mA; 15 kV). The use of this different X-ray source was employed since enhanced photoelectron intensity was significantly more important than avoiding artifacts due to X-ray satellites. In select regions of interest, further focusing was performed to yield well defined features. Most of the images and data presented in Figs. 2–4 and in the Supporting Information (SI) were taken at pass energy 40 eV over an area of 216 μm × 216 μm to improve both energy and spatial resolution. Unless otherwise noted, images were acquired at uniformly spaced energy intervals over the C(1s) energy range for a constant acquisition time per image for all MWCNT composite spots analyzed. For the details of the settings of both spectroscopy and imaging, refer to section I of the SI.

2.3. XPS image analysis

The non-uniform shape of the MWCNT aggregates required a new image analysis procedure to generate image masks for the MWCNT-rich and the epoxy-rich composite components. The MWCNT-rich image mask (conductive mask) identified groups of pixels having predominantly spectral characteristics of the MWCNT and separated them from the remaining pixels. The epoxy-rich image mask (non-conductive mask) was identified as the remaining pixels less an interfacial border. Regions of interest (ROIs) were identified by thresholding summed images based on MWCNT signals. The binary image created from these pixels was then dilated (expanded) and eroded (shrank) to yield an image mask that contained a small number of large, contiguous ROIs defining the MWCNT-rich, conductive regions while eliminating isolated spikes and minimums in intensity, such as pixels caused by measurement noise and deemed unphysical (Fig. 3, center). Once the conductive image mask is established, a non-conductive image mask was formed by dilating the conductive ROIs and inverting the mask. This yields two image masks that accept most of the data, but exclude a transition region between the conductive ROIs and the epoxy-rich composite of lower conductivity (Fig. 3, right). The transition region that is excluded from both masks avoids analysing the region of mixed MWCNT-rich and epoxy-rich signals. These masks were then applied to each image to calculate total intensity at the binding energy of acquisition, normalized to number of accepted pixels for the mask. This information was then compiled into a C(1s) spectra generated by plotting intensity/pixel vs binding energy. This combined procedure for image processing and spectral generation was performed in Mathematica. The code, additional comments and information, is provided as SI (SI section 2, Fig. S2(A)–4(A), Fig. S5 in the SI).

2.4. Raman spectroscopy

Raman spectral imaging was performed on a Renishaw InVia Raman Microscope (Hoffman Estates, IL) on the 5% MWCNT composite. Images were acquired using a 785 nm laser through a 5 × objective in 180° backscatter configuration. Raman spectra, from 1200 cm^{-1} to 1700 cm^{-1}, were acquired every 20 μm across a predefined region of the sample to create an image. This spectral window covers the Raman D, or defect, peak and the G, or graphitic, peak of the carbon nanotubes. After data acquisition, Matlab (Natick, MA) was used for analysis and stitching of the image.

2.5. Scanning electron microscopy

A Helios 650 NanoLab Focused Ion Beam (FIB) SEM from FEI (Hillsboro, OR) was used for SEM imaging. The sample was mounted on a 10 mm aluminum pin stub using a double sided carbon tab. Images were taken using 2 keV electron beam energy, (100–800) pA probe beam current, 4 mm working distance and Everhardt-Thornly detector in secondary electron mode.

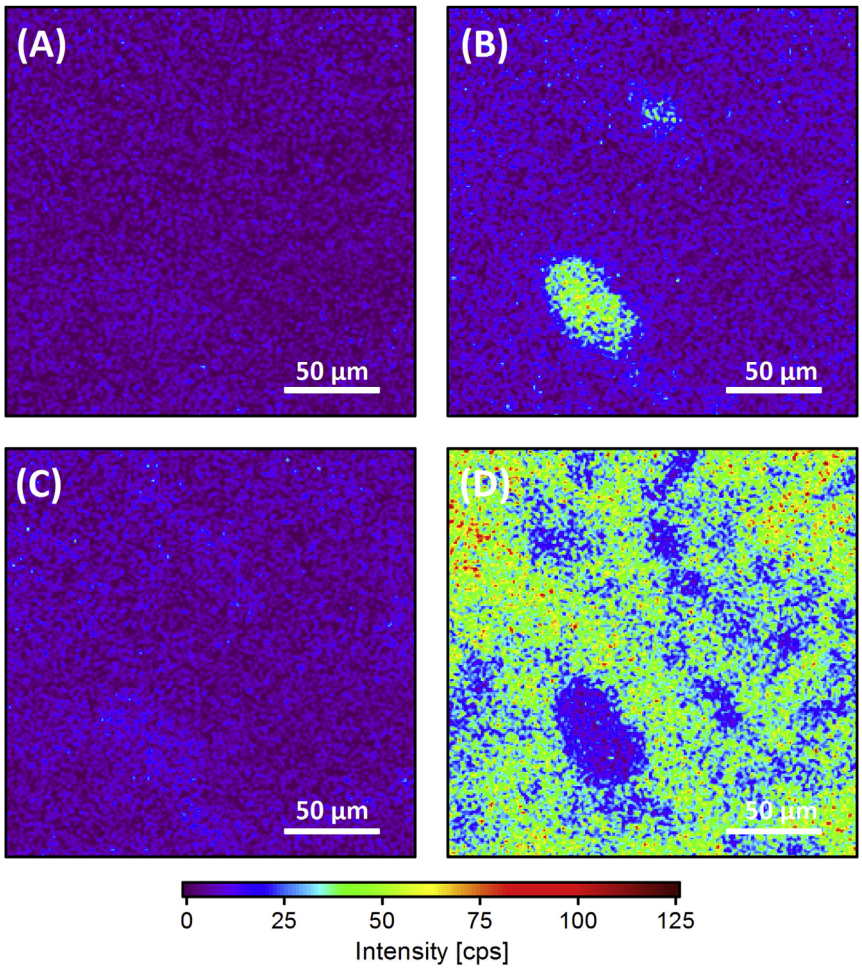

Fig. 2. High spatial resolution XPS imaging of a nominally 1% MWCNT composite measured at (A) 282 eV, (B) 285 eV, (C) 289 eV and (D) 294 eV. (Mg Kα = 405 W). (A color version of this figure can be viewed online.)

3. Results and discussions

3.1. XP spectral characterization and differential charging

After preparation of the sample's surface was completed, traditional X-ray photoelectron spectra were acquired for all specimens, plus epoxy and MWCNT control specimens (See Fig. 1 and SI Fig. S1) to demonstrate the different electronic characteristics of pure epoxy samples, varying percentages of MWCNT composites, and 100% MWCNT controls. Initial wide range survey spectra (0–700) eV demonstrated the poor conductivity of the epoxy (0%) as evident by the large shift of >300 eV from the typical C(1s) binding energy (Fig. 1(A), bottom). Additionally, the peak shapes were drastically distorted, also consistent with a charging sample. To clearly resolve any features from the pure epoxy, the surface had to be charge neutralized using an electron flood source which typically overcompensates a positive bias with a constant negative bias (SI Fig. S1B). Therefore, the uncorrected, neutralized spectra for epoxy revealed a peak maximum at ≈282 eV, representative of the hydrocarbon fraction. When MWCNT were added to the epoxy, the C(1s) peak position for the composites decreased in binding energy to values closer to the literature values of hydrocarbons and MWCNT carbon (graphitic) [25]. This was more clearly observed in the high resolution, C(1s) spectra presented in Fig. 1(B) for all MWCNT composites. These findings are qualitatively consistent with previous measurements of weathered MWCNT composites [34] that demonstrated dissipation of surface charge increases with surface concentration of MWCNT. Regardless, significant charging was still evident even with the addition of MWCNT.

Two distinct features can be identified in the high resolution C(1s) spectra of Fig. 1(B) consistent with differential charging: (1) a dominant feature at a higher, variable binding energy and (2) a minor feature at a fixed binding energy indicated by the vertical dotted line. Spectral feature (1) was identified as the charging feature associated with poorly-conducting, epoxy-rich composites consistent with previous reports [17,25,34]. This peak shifts to lower binding energies with increased MWCNT concentration. For 1% MWCNT composites, the peak position was (299.2 ± 0.5) eV, while at 5% MWCNT the charge peak maximum had shifted to a peak position of (290.4 ± 0.2) eV. Although the charging peak's binding energy continued to decrease with increasing MWCNT concentration, it was not observed to reach its fully neutralized binding energy in this study. The second spectral feature in the C(1s) region was present at a similar binding energy, (284.4–284.5) eV, for each concentration of MWCNT composite analyzed, as indicated by the vertical dotted line in Fig. 1(B). The conductive spectral feature is identified as MWCNT at the surface and has a comparable peak position in the 100% control spectra. Since the MWCNT are more conductive than epoxy, we observed differential charging. This difference in conductivity between MWCNT and polymeric materials such as epoxy has been previously

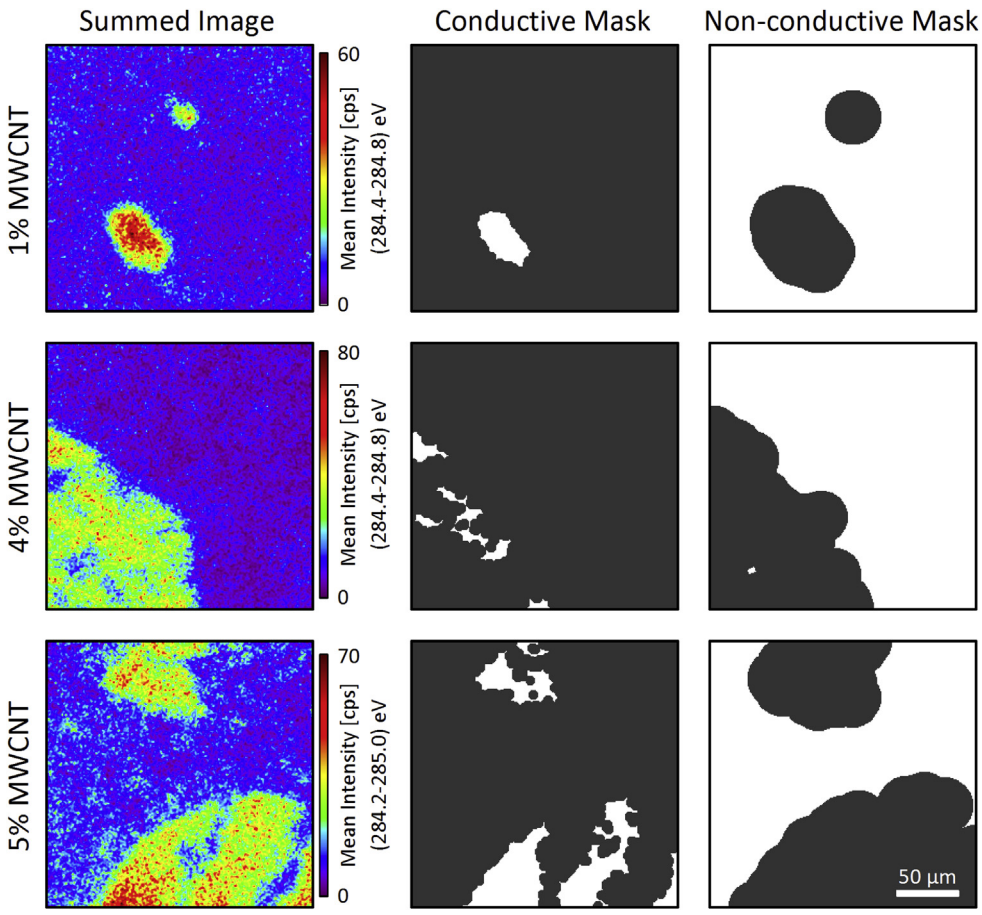

Fig. 3. XPS image for the 1% (top row), 4% (middle row) and 5% (bottom row) MWCNT composites. Summed images (left column) were formed between (284.25–285) eV for 1% MWCNT and (284.4–284.8) eV for 4% and 5% MWCNT from which the top 50% of pixels were selected, respectively, to generate a conductive image mask (center column). A non-conductive image mask was also generated (right column) which counted all pixels not included the conductive image mask less a 'border' region. (Scale bar in the lower right applies to all images). (A color version of this figure can be viewed online.)

demonstrated in the literature [10,11]. Qualitatively, one can observe an increase in the intensity of the peak with the increased MWCNT composition. We propose that the peak shift in the charging feature is a consequence of the increased conductivity of the composite as the MWCNT loading increased. This finding is consistent with previous studies which include measurements of MWCNT and epoxy alone as well as in composite form [35–39]. We further propose that the static, MWCNT peak is in part due to large aggregates at the composite surface.

3.2. *MWCNT aggregates observable by imaging XPS*

To assess if there were any micrometer scale MWCNT aggregates in the composites, hyperspectral XPS imaging was conducted. Images were collected across the C(1s) region's energy range every 0.2 eV for the 4% and 5% MWCNT composites and every 0.3 eV or 0.25 eV for the 1% MWCNT composite. The energy range and step size were based on results shown in Fig. 1 and detailed instrumental settings information may be found in section I of the SI.

Example XPS images from the 1% MWCNT composite in Fig. 2 demonstrate the effectiveness of employing XPS imaging on differentially charging surfaces to examine dispersion quality. Fig. 2(A–D) present four images acquired at four different binding energies that are part of a set of images acquired over a range of 280.1 eV–300.5 eV Fig. 2(A) shows data acquired at a lower binding energy (282 eV) which yields an image of uniformly low signal, devoid of any significant features. Compared to the background of 2(A), the image acquired at 285 eV (Fig. 2(B)) reveals two localized regions of enhanced photoelectron intensity. These ROIs both have dimensions less than 100 µm and are attributed to the conductive MWCNT-rich signal observed in Fig. 1(B). The image acquired at 289 eV (Fig. 2(C)) is largely featureless, with photoelectron intensity similar to 2(A). Lastly, significant photoelectron intensity is observed across the entire image acquired at 294.0 eV (Fig. 2(D)), presumably due to the charging peak location, with the notable exception of a depression in signal in the lower left quadrant. The depression in charging intensity is consistent with the large conductive feature observed in Fig. 2(B) and provides further evidence of a MWCNT-rich region. A more complete series of images collected for 1% MWCNT composites can be found in the SI (Fig. S2(A)). The reasons for deviation in binding energies from those shown in Fig. 1 and S2 will be described in later sections.

Fig. 3 represents the image processing procedure developed to analyze the hyperspectral XPS imaging and separate the differentially charging regions for the 1% MWCNT composites observed in Fig. 2 as well as 4% and 5% MWCNT composites. The left column of Fig. 3 illustrates this in the form of a summed image. Summed images were generated by averaging contiguous, evenly spaced, XPS images between 284.25 eV and 285 eV to enhance the signal-to-noise ratio of the image (see Fig. 3 caption for more details) and improve the quality of spatial separation between the conductive and non-conductive surface. The high intensity regions in Fig. 2(B)

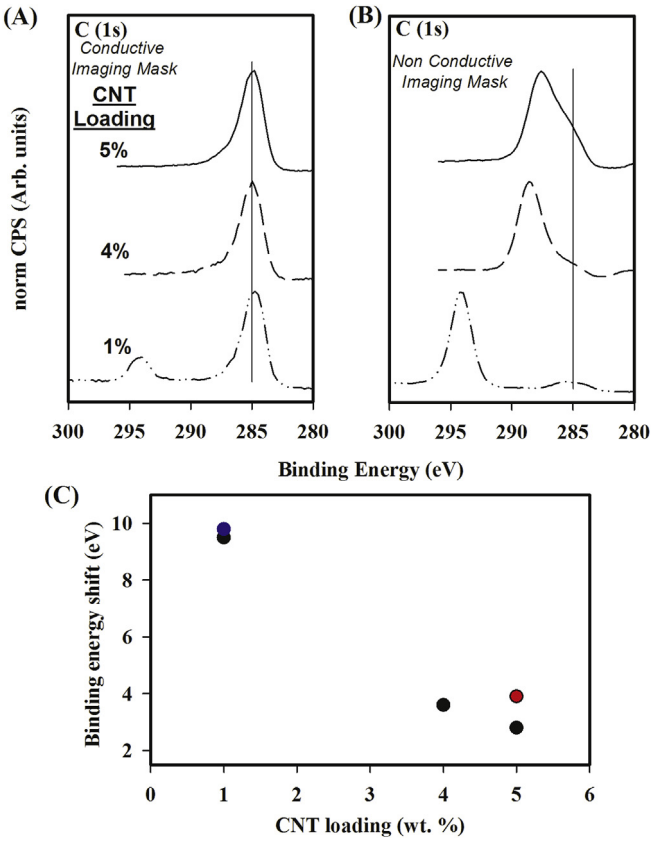

Fig. 4. Spectra generated from hyperspectral imaging obtained by applying the (A) conductive and (B) non-conductive imaging masks to the 1%, 4% and 5% MWCNT composites. (C) Binding energy positions for non-conductive and conductive peak maximums plotted versus MWCNT loading. (Legend: Solid symbols: Non-conductive measurements. Open symbols: Conductive measurements. Squares, diamonds and triangles are from different areas of the same sample under different conditions. See SI for experimental details). (A color version of this figure can be viewed online.)

and Fig. 3 (left) correspond to the spectral feature associated with higher electrical conductivity consistent with MWCNT-rich ROIs.

Because the geometric shape of the ROIs is complex, an image processing procedure was required to separate the spectral information for the two spatial regions (conductive, MWCNT-rich and non-conductive, epoxy-rich). A script was written to process the C(1s) energy region images by selecting ROIs based on thresholding the summed images presented in the left column of Fig. 3. This produced conductive masks (center column of Fig. 3) which were based on all pixels with intensity greater than 50% of the maximum signal intensity, with some additional image processing that is described in the SI. The conductive masks represent ROIs that are rich in MWCNT (*e.g.,* aggregates) and therefore possess improved electrical conductivity by forming an interlinking network capable of dissipating charge. This phenomena has been previously exploited in the literature for individual nanotubes in a polyimide matrix using SEM and EFM [42]. A non-conductive mask (right column of Fig. 3) representing the epoxy-rich ROI was created by dilating the conductive mask by 25 pixels and inverting the result. This dilation created a border that represented intermediate regions where both MWCNT-rich aggregates and epoxy-rich composite regions may co-exist (See SI for further explanation). These border pixels, or transition region, are not included in subsequent image analysis to avoid mixing MWCNT-rich with epoxy-rich ROIs, thereby providing the best chance of acquiring C(1s) spectra of only aggregates or composite, respectively.

Fig. 4 demonstrates the results of applying this image processing procedure to XPS images acquired on 1%, 4% and 5% MWCNT composites which were allowed to differentially charge. The image masks were applied to each MWCNT composite hyperspectral image series to acquire a C(1s) spectrum from the MWCNT composite. This was achieved by calculating an average intensity/pixel for pixels within each mask. This yielded a photoelectron intensity/pixel attributed to the binding energy at which the image was acquired. By applying this script to each energetically unique image for a given MWCNT composite, two spectra could be extracted that represent the C(1s) energy region of the MWCNT rich (Fig. 4(A)) and epoxy rich (Fig. 4(B)) areas defined by the image masks in Fig. 3. The spectra in Fig. 4(A) are dominated by a C(1s) spectral feature at 284.8 eV–285.0 eV with an asymmetric line shape which tails off towards a flat baseline near 290 eV–291 eV. This is consistent with the C(1s) line shape for pure MWCNT, as has been seen previously in the literature [25,34] and in the control measurements (See SI Fig. S1) and suggests that the ROIs defined by the conductive masks are dominated by MWCNT. Furthermore, it was not comparable to the epoxy neutralized control. An additional spectral feature is observed at a binding energy of 294 eV–295 eV for the 1% MWCNT loading which is attributed to the epoxy-rich composite as is consistent with Fig. 4(B).

The non-conductive mask was employed to generate additional C(1s) spectra for comparison, as seen in Fig. 4(B). The non-conductive spectra are different from their conductive counterparts, as evidenced by the shift to higher binding energy due to significant charging. This observed shift from the 285.0 eV peak observed in Fig. 4(A) increased with decreased MWCNT loading. The 4% and 5% MWCNT composites are characterized by a charge peak maximum near 287.6 eV and 288.6 eV, respectively, and also have clear evidence of broadening above the baseline at 285.0 eV in the form of a shoulder. This intensity at 285.0 eV could be due to any combination of the following: 1) the presence of regions of MWCNT composite where the concentration and percolation of the nanotubes is sufficient to eliminate charging; 2) small spatial regions of high MWCNT concentrations that are too small to resolve in XPS images but are sufficient to provide conductive pathways; and/or 3) charge induced tailing towards lower binding energies. In the case of the 1% MWCNT composites, the non-zero contributions around 285.0 eV are more easily explained by the presence of X-ray source satellites. Specifically, Mg Kα X-rays have contributions at +8.4 eV and +10.1 eV from their main line at 1253.6 eV, resulting in contributions of 8.0% and 4.1%, respectively, at lower binding energies [43]. This is consistent with observations and accounts for the majority of the 1% MWCNT composite signal in Fig. 4(B) around 285 eV.

Further observations reveal discrepancies when comparing the charge peak position in the C(1s) regions of Fig. 4(B) and Fig. 1(B). Indeed, Fig. 1(B) suggests that the epoxy-rich composite areas collected as spectra are charging to a greater degree than the imaged location represented by Fig. 4(B). While this could represent heterogeneity across the sample, it is more likely attributed to the different X-ray sources which are known to vary when samples charge. Some reasons for a lesser degree of differential charging associated with Mg X-rays as opposed to monochromatic Al include the following: higher X-ray energies [33], the spatial heterogeneity of X-ray flux [31], and the potential for low level charge neutralization due to secondary electrons emanating from the thin window separating the Mg X-ray source from the chamber which is in line of sight to the sample.

The enhancement in the composite's overall conductivity due to increased MWCNT contributions can be more easily observed in Fig. 4(C), which plots the peak maxima for each set of C(1s) regions as a function of MWCNT loading. Additional measurements were included in this plot from the each MWCNT loadings from different

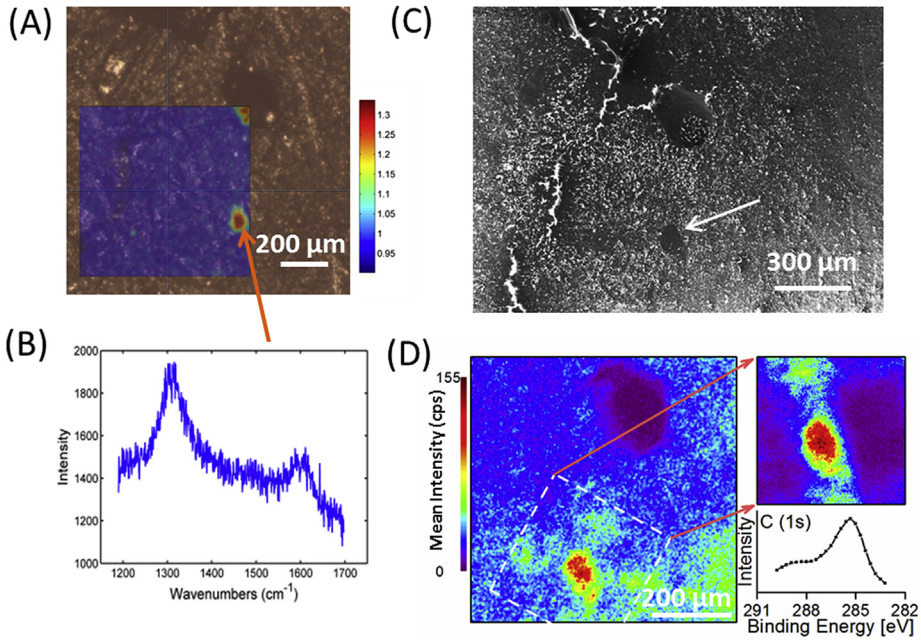

Fig. 5. (A) Raman imaging heat map overlaid on an optical microscopy image of the 5% MWCNT composite. Heat map reflects the ratio of the D-peak at 1300 cm^{-1} to the background intensity at 1200 cm^{-1}. Warmer colors represent more MWCNT. Raman ratio scale is to the right. (B) Example Raman spectrum from MWCNT-rich regions highlighting the D and G Raman bands. (C) SEM image of the same position on the 5% MWCNT composite. The arrow indicates a region of low charge buildup consistent with the Raman location of the MWCNT-rich area. (D) XPS summed image of the same position using a large area of analysis (left) and a medium area of analysis (upper right) (both on same scale). Imaging spectra (lower right) extracted from the medium area of analysis (see SI for XPS experimental details). (A color version of this figure can be viewed online.)

spots on the composite. This plot demonstrates that the peak maximum for the non-conductive C(1s) region (Fig. 4B) consistently decreases in binding energy with increased MWCNT loading while the peak maximum for the conductive C(1s) region (Fig. 4(A)) remains relatively constant near 285 eV. This provides evidence that the addition of a greater mass fraction of nanotubes results in the improvement of electrical conductivity in the epoxy-rich portions of the MWCNT composites while still maintaining clear regions of aggregation. This finding is consistent with other studies which have demonstrated enhancements in overall conductivity for MWCNT-epoxy composites with increased nominal nanomaterial loading using 2 and 4 point probe measurements [44]. Based on this, we can assume that there is a MWCNT component to the epoxy-rich region which is consistent with our assertion that the non-conductive area is representative of well dispersed composite. Lastly, the variation in the 5% MWCNT composites suggests a decreased uniformity in the well dispersed composite's nanotube concentrations as the mass fraction of MWCNT increases. However, this question requires further study in order to be addressed. Additional work will also be needed to extract semi-quantitative values, such as relative percentages of surface carbon from different materials, from the processed images.

3.3. Confirmation of XPS results by orthogonal imaging techniques

The 5% MWCNT composite was studied and tested with XPS, Raman spectroscopy and SEM imaging on the same region of the surface using the surrounding topography of the sample as a source of fiducial markers to identify the location for analysis. These orthogonal techniques confirm the presence of localized regions of high MWCNT concentrations at the surface, as presented in Fig. 5. Raman imaging (color) is presented as an overlay on an optical microscope image in Fig. 5(A). The overlay is a 700 µm square heat map of the ratio of the Raman defect (D) peak intensity at ≈1300 cm^{-1}, to the background intensity at 1200 cm^{-1}. The defect peak at 1300 cm^{-1} is one of the dominant Raman features of MWCNT and arises from defects in the graphene lattice. As seen in Fig. 5(A), there are localized regions of higher ratio (D-peak/noise) in two distinct regions imaged. An example of the Raman spectrum from this MWCNT-rich region is provided in Fig. 5(B) which shows increased intensity at both the Raman D peak region near 1300 cm^{-1} and at the G (graphitic) peak region around 1600 cm^{-1} relative to the baseline, as is consistent with literature examples of MWCNT [45]. In a second heat map presented in the SI (Fig. S5), a spectrum of the dark blue background is presented which, while being higher in absolute intensity is devoid of any evidence of the D and G bands that are specific to the MWCNT. The second hotspot, which is more clearly observed in SI Fig. S5, was in a pit on the sample surface (upper right corner) and was used as the fiducial marker.

The SEM image in Fig. 5(C) was obtained after scanning the same region of interest continuously for a few mins. This results in build-up of negative charge on the sample surface where there are epoxy-rich composite phases; as evident by the bright phases in Fig. 5(C). The dark phase (see arrow in Fig. 5(C)) represents a more conductive regime in the composite, presumably due to a region of greater MWCNT concentration, where incident electrons are more effectively transported away from the surface via the interconnected subsurface MWCNT network. The fiducial marker (pit) directly above this region also appeared dark, which is also consistent with the assertion that the pit had a localized high concentration of MWCNT. While electron microscopy images were not acquired for individual MWCNT in this specific region of the 5% MWCNT composite, other regions were located on the same sample and imaged which provided evidence of their presence (See SI Fig. S6).

Large XPS images were also taken of the same region, as displayed by the summed image (284.5 eV–285.5 eV) on the left of Fig. 5(D) (See SI for details). Again, the pit served as the fiducial marker (top center of the summed image) and was present in every single image as a complete lack of signal. This is presumably due to the attenuation of the X-rays coming in at an angle of 60° to the

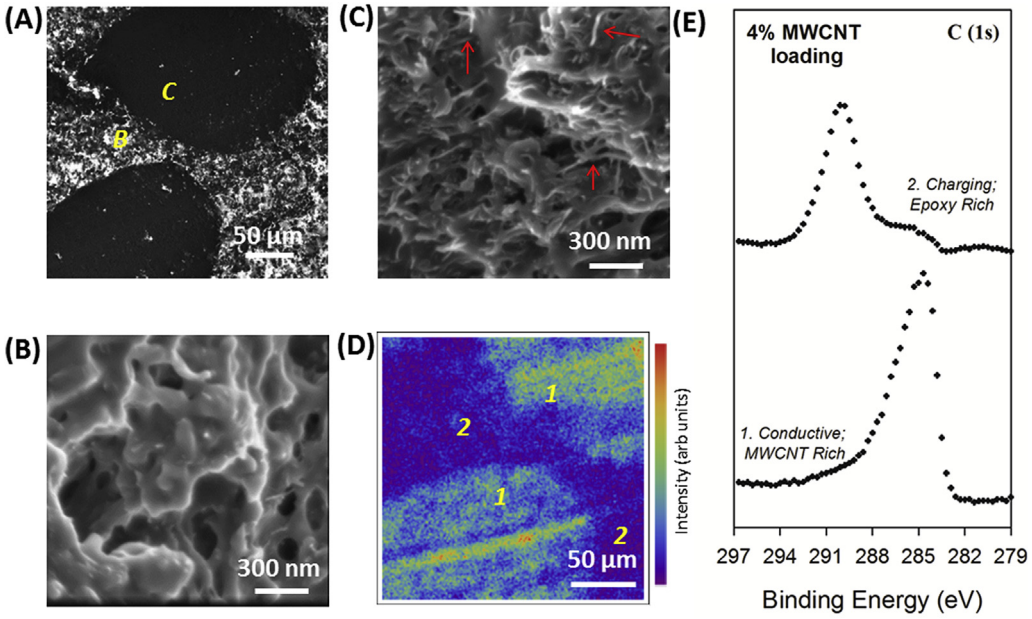

Fig. 6. SEM and XPS images of 4% MWCNT composites. (A) Large scale SEM image of MWCNT composite with 2 localized regions of conductivity (dark) separated by charging regions (bright) as was observed in Fig. 5(C). (B) Region indicated in 6(A) of high charging is characterized by an irregular surface *mostly* devoid of tube-like structures. (C) Region indicated in 6(A) of high conductivity is characterized by a surface with many interconnected tube-like MWCNT structures. (D) XPS summed image of the composite surface in the same location as 6(A) with regions of high intensity notated with a *1.* reflective of MWCNT-rich, conductive regions and those notated with a *2.* are reflective of an epoxy rich, charging region. (E) Extracted regions of the C(1s) spectra reflective of the conductive and insulating carbon found in 6 (D). (A color version of this figure can be viewed online.)

surface normal. Regardless, the summed image demonstrates a clear local maximum in intensity lower on the image in a summed image representative of the MWCNT-rich domain.

A higher spatial resolution image set was acquired every 0.3 eV from 283.2 eV to 289.8 eV under different analyzer conditions (See SI for details), which is represented as a summed image in the upper right of Fig. 5(D). A conductive spectrum is shown in the lower right corner of Fig. 5(D) which is characterized by the asymmetric line shape and a peak maximum at 285.3 eV which is consistent with previous results. The spectra obtained from application of the non-conductive mask demonstrated the presence of a charge feature at 289.2 eV (Data not shown). Image processing conditions can be found in the SI (SI section 2 and Fig. S7).

Acquisition of additional SEM images in conjunction with XPS imaging can be observed in Fig. 6 and were acquired to further confirm the identity of spatially separated, conductive regions using the 4% MWCNT composites. Fig. 6(A) demonstrates a comparable result with Fig. 5(C). Specifically, the darker, more conductive regions representing the MWCNT rich regions, and brighter, more insulating regions representing charge build up and less MWCNT characteristics can clearly be observed. As marked in Fig. 6(A), Fig. 6(B and C) represent zoomed in SEM images of low and high MWCNT surface concentrations, respectively. While only a couple of MWCNT can be observed at the surface for the MWCNT poor regions, the MWCNT rich regions can be characterized by a large amount of interconnecting, tube-like structures, which are presumably individual MWCNT and/or bundles. These can be more clearly observed in SI Fig. S8 which provides a blow up of this image. Fig. 6(D) is a summed XPS image (5 images from 283.8 eV to 285 eV) of the same region presented in 6(A). The conductive, MWCNT-rich regions are indicated with a '*1*' while the charging, epoxy-rich regions are indicated with a '*2*'. Fig. 6(E) presents the spectra yielded from the in-house image processing software for the regions of different conductivity which is consistent with Fig. 4(A) and (B).

By taking advantage of the different electrical properties of MWCNT and epoxy, XPS imaging clearly provides a useful means of identifying heterogeneities in MWCNT composites, specifically within the top 10 nm. This can provide an alternative tool for understanding interfacial properties which may impact the potential for nanoparticle release. Additionally, imaging XPS could be employed as a tool to more accurately identify locations of interest for small spot analysis in XPS spectroscopy, a tool which could also be employed in other composite systems to search for aggregates. SEM imaging provides further physical support for XPS imaging capabilities while Raman imaging provided chemical confirmation of MWCNT aggregate structures. The different information obtained from all three of these analytical techniques has the potential to construct a more complete story both chemically and physically regarding the physico-chemical characteristics than any one of them can perform alone highlighting the benefit of employing orthogonal approaches.

4. Conclusions

This study demonstrates how XPS imaging can be effectively employed in the characterization of MWCNT composites by exploiting differential charging. This technique provides qualitative physical information on the quality of the nanomaterial dispersion within the epoxy; electrical information regarding the impact of additional MWCNT on the conductivity of the composite; and chemical information regarding the identity of the conductive regions. Raman imaging and SEM have been successfully employed as orthogonal techniques confirming the XPS-based observations. This technique is promising as a characterization tool for environmental and toxicological issues of nanotube-based composites and may be applicable to other polymer-based composites with other conductive carbon-based nanomaterial fillers. Future characterization studies will further improve the measurement in order to obtain more quantitative information.

Appendix A. Supplementary data

Supplementary data related to this article can be found at http://dx.doi.org/10.1016/j.carbon.2015.10.073.

References

[1] X. Sui, H.D. Wagner, Tough nanocomposites: the role of carbon nanotube type, Nano Lett. 9 (4) (2009) 1423–1426.
[2] P. Patel, MIT Technol. Rev. (2009). http://www.technologyreview.com/news/411751/clear-carbon-nanotube-films/.
[3] Z. Spitalsky, D. Tasis, K. Papagelis, C. Galiotis, Carbon nanotube–polymer composites: chemistry, processing, mechanical and electrical properties, Prog. Polym. Sci. 35 (3) (2010) 357–401.
[4] M. Bansal, R. Srivastava, C. Lal, M.N. Kamalasanan, L.S. Tanwar, Carbon nanotube-based organic light emitting diodes, Nanoscale 1 (3) (2009) 317.
[5] Q. Li, Q. Xue, L. Hao, X. Gao, Q. Zheng, Large dielectric constant of the chemically functionalized carbon nanotube/polymer composites, Compos. Sci. Technol. 68 (10–11) (2008) 2290–2296.
[6] Y. Shen, G. Liang, L. Yuan, Z. Qiang, A. Gu, Unique Li0.3Ti0.02Ni0.68O-carbon nanotube hybrids: synthesis and their epoxy resin composites with remarkably higher dielectric constant and lower dielectric loss, J. Alloys Compd. 602 (2014) 16–25.
[7] J.K.W. Sandler, J.E. Kirk, I.A. Kinloch, M.S.P. Shaffer, A.H. Windle, Ultra-low electrical percolation threshold in carbon-nanotube-epoxy composites, Polymer 44 (19) (2003) 5893–5899.
[8] H. Liu, Y. Shen, Y. Song, C.-W. Nan, Y. Lin, X. Yang, Carbon nanotube array/polymer core/shell structured composites with high dielectric permittivity, low dielectric loss, and large energy density, Adv. Mater. 23 (43) (2011) 5104–5108.
[9] J. Zhang, L.-B. Kong, B. Wang, Y.-C. Luo, L. Kang, In-situ electrochemical polymerization of multi-walled carbon nanotube/polyaniline composite films for electrochemical supercapacitors, Synth. Met. 159 (3–4) (2009) 260–266.
[10] L.-C. Tang, Y.-J. Wan, K. Peng, Y.-B. Pei, L.-B. Wu, L.-M. Chen, L.-J. Shu, J.-X. Jiang, G.-Q. Lai, Fracture toughness and electrical conductivity of epoxy composites filled with carbon nanotubes and spherical particles, Compos. Part A Appl. Sci. Manuf. 45 (2013) 95–101.
[11] H.J. Dai, E.W. Wong, C.M. Lieber, Probing electrical transport in nanomaterials: conductivity of individual carbon nanotubes, Science 272 (5261) (1996) 523–526.
[12] D.M. Mitrano, S. Motellier, S. Clavaguera, B. Nowack, Review of nanomaterial aging and transformations through the life cycle of nano-enhanced products, Environ. Int. 77 (2015) 132–147.
[13] M.F.L. De Volder, S.H. Tawfick, R.H. Baughman, A.J. Hart, Carbon nanotubes: present and Future commercial applications, Science 339 (6119) (2013) 535–539.
[14] D.R. Baer, M.H. Engelhard, G.E. Johnson, J. Laskin, J. Lai, K. Mueller, P. Munusamy, S. Thevuthasan, H. Wang, N. Washton, A. Elder, B.L. Baisch, A. Karakoti, S.V.N.T. Kuchibhatla, D. Moon, Surface characterization of nanomaterials and nanoparticles: important needs and challenging opportunities, J. Vac. Sci. Technol. A Vac. Surfaces, Films 31 (5) (2013) 050820.
[15] C.M. Sayes, D.B. Warheit, Characterization of nanomaterials for toxicity assessment, Wiley Interdiscip. Rev. Nanomed. Nanobiotech. 1 (6) (2009) 660–670.
[16] J.C. Vickerman and I.S. Gilmore, 2nd ed. Series. 2009, Chichester, U.K.: Wiley. xix, 666 pp.
[17] J.M. Gorham, T. Nguyen, C. Bernard, D. Stanley, R.D. Holbrook, Photo-induced surface transformations of silica nanocomposites, Surf. Interface Analysis 44 (13) (2012) 1572–1581.
[18] T. Nguyen, B. Pellegrin, C. Bernard, X. Gu, J.M. Gorham, P. Stutzman, D. Stanley, A. Shapiro, E. Byrd, R. Hettenhouser, J. Chin, Fate of nanoparticles during life cycle of polymer nanocomposites, J. Phys. Conf. Ser. 304 (2011) 012060.
[19] T. Nguyen, B. Pellegrin, C. Bernard, S. Rabb, P. Stuztman, J.M. Gorham, X. Gu, L.L. Yu, J.W. Chin, Characterization of surface accumulation and release of nanosilica during irradiation of polymer nanocomposites by ultraviolet light, J. Nanosci. Nanotechnol. 12 (8) (2012) 6202–6215.
[20] W. Wohlleben, G. Vilar, E. Fernandez-Rosas, D. Gonzalez-Galvez, C. Gabriel, S. Hirth, T. Frechen, D. Stanley, J. Gorham, L.-P. Sung, H.-C. Hsueh, Y.-F. Chuang, T. Nguyen, S. Vazquez-Campos, A pilot interlaboratory comparison of protocols that simulate aging of nanocomposites and detect released fragments, Environ. Chem. 11 (4) (2014) 402.
[21] J.M. Gorham, K. Murphy, J. Liu, D. Tselenchuk, G. Stan, T.M. Nguyen, R.D. Holbrook, M. Winchester, R.F. Cook, R.I. MacCuspie, V.A. Hackley, Preparation of Silver Nanoparticle Loaded Cotton Threads to Facilitate Measurement Development for Textile Applications 1200-8, in: NIST Technical Series: SP 1200–8, 2015.
[22] N. Alissawi, V. Zaporojtchenko, T. Strunskus, T. Hrkac, I. Kocabas, B. Erkartal, V.S.K. Chakravadhanula, L. Kienle, G. Grundmeier, D. Garbe-Schönberg, F. Faupel, Tuning of the ion release properties of silver nanoparticles buried under a hydrophobic polymer barrier, J. Nanoparticle Res. 14 (7) (2012).
[23] J.M. Gorham, R.I. MacCuspie, K.L. Klein, D.H. Fairbrother, R.D. Holbrook, UV-induced photochemical transformations of citrate-capped silver nanoparticle suspensions, J. Nanoparticle Res. 14 (10) (2012).
[24] S. Zanna, C. Saulou, M. Mercier-Bonin, B. Despax, P. Raynaud, A. Seyeux, P. Marcus, Ageing of plasma-mediated coatings with embedded silver nanoparticles on stainless steel: an XPS and ToF-SIMS investigation, Appl. Surf. Sci. 256 (22) (2010) 6499–6505.
[25] J.M. Gorham, J.W. Woodcock, K.C. Scott, Challenges, Strategies and Opportunities for Measuring Carbon Nanotubes within a Polymer Composite by X-ray Photoelectron Spectroscopy: 1200-10, in: NIST Technical Series: SP 1200–10, National Institute of Standards and Technology, Gaithersburg, MD, 2015.
[26] A.V. Naumkin, A.K. Kraut-Vass, S.W. Garenstroom, C.J. Powell, in: NIST Standard Reference Database 20, Version 4.1, National Institute of Standards and Technology, 2012.
[27] K.A. Wepasnick, B.A. Smith, J.L. Bitter, D. Howard Fairbrother, Chemical and structural characterization of carbon nanotube surfaces, Anal. Bioanal. Chem. 396 (3) (2010) 1003–1014.
[28] D.G. Goodwin, K.M. Marsh, I.B. Sosa, J.B. Payne, J.M. Gorham, E.J. Bouwer, D.H. Fairbrother, Interactions of microorganisms with polymer nanocomposite surfaces containing oxidized carbon nanotubes, Environ. Sci. Technol. 49 (9) (2015) 5484–5492, 150413133334006.
[29] A.J. Barlow, O. Scott, N. Sano, P.J. Cumpson, Multivariate auger feature imaging (MAFI) – a new approach towards chemical state identification of novel carbons in XPS imaging, Surf. Interface Analysis 47 (2) (2015) 173–175.
[30] S. Suzer, Differential charging in X-ray photoelectron spectroscopy: a nuisance or a useful tool? Anal. Chem. 75 (24) (2003) 7026–7029.
[31] B.J. Tielsch, J.E. Fulghum, Differential charging in XPS .1. Demonstration of lateral charging in a bulk insulator using imaging XPS, Surf. Interface Anal. 24 (6) (1996) 422–427.
[32] B.J. Tielsch, J.E. Fulghum, Differential charging in XPS .3. A comparison of charging in thin polymer overlayers on conducting and non-conducting substrates, Surf. Interface Anal. 25 (11) (1997) 904–912.
[33] B.J. Tielsch, J.E. Fulghum, D.J. Surman, Differential charging in XPS .2. Sample mounting and x-ray flux effects on heterogeneous samples, Surf. Interface Anal. 24 (7) (1996) 459–468.
[34] E.J. Petersen, T. Lam, J.M. Gorham, K.C. Scott, C.J. Long, D. Stanley, R. Sharma, J.A. Liddle, B. Pellegrin, T. Nguyen, Methods to assess the impact of UV irradiation on the surface chemistry and structure of multiwall carbon nanotube epoxy nanocomposites, Carbon 69 (2014) 194–205.
[35] T.W. Ebbesen, H.J. Lezec, H. Hiura, J.W. Bennett, H.F. Ghaemi, T. Thio, Electrical conductivity of individual carbon nanotubes, Nature 382 (6586) (1996) 54–56.
[36] A. Allaoui, S. Bai, H.M. Cheng, J.B. Bai, Mechanical and electrical properties of a MWNT/epoxy composite, Compos. Sci. Technol. 62 (15) (2002) 1993–1998.
[37] S.K. Sharma, R.P. Tandon, V.K. Sachdev, Pre-localized MWCNT network for a low percolation threshold in MWCNT/ABS nanocomposites: experiment and theory, RSC Adv. 4 (105) (2014) 60733–60740.
[38] V. Choudhary, B.P. Singh, R.B. Mathur, Carbon Nanotubes and Their Composites, 2013.
[39] T.V. Kosmidou, Structural, mechanical and electrical characterization of epoxy-amine/carbon black nanonocomposites, eXPRESS Polym. Lett. 2 (5) (2008) 364–372.
[40] C.S. Davis, J.W. Woodcock, J.W. Gilman, Preparation of Nanoscale Multi-walled Carbon Nanotube Dispersions in a Polyetheramine Epoxy for Eco-toxicological Assessment, in: NIST Technical Series: SP 1200–9, 2015.
[41] S.C. Barron, J.M. Gorham, M.P. Patel, M.L. Green, High-throughput measurements of thermochromic behavior in V1–xNbxO2 combinatorial thin film libraries, ACS Comb. Sci. 16 (10) (2014) 526–534.
[42] M. Zhao, B. Ming, J.-W. Kim, L.J. Gibbons, X. Gu, T. Nguyen, C. Park, P.T. Lillehei, J.S. Villarrubia, A.E. Vladár, J. Alexander Liddle, Erratum: new insights into subsurface imaging of carbon nanotubes in polymer composites via scanning electron microscopy (2015 Nanotechnology 26085703), Nanotechnology 26 (16) (2015) 169601.
[43] J.F. Moulder; W.F. Stickle; P.E. Sobol; and K.D. Bomben, Series, ed. J. Chastain. 1995, Eden Prairie: Perkin-Elmer Corporation.
[44] C.S. Davis, N.D. Orloff, J.W. Woodcock, C.J. Long, K.A. Twedt, B. Natarajan, J.E. Seppala, J.J. McClelland, J. Obrzut, J.A. Liddle, J.W. Gilman, Cure Temperature Influences Composite Electrical Properties via Carbon Nanotube-rich Domain Formation, submitted to Carbon, 2015.
[45] S. Osswald, M. Havel, Y. Gogotsi, Monitoring oxidation of multiwalled carbon nanotubes by Raman spectroscopy, J. Raman Spectrosc. 38 (6) (2007) 728–736.